ARTICLES
https://doi.org/10.1038/s41565-022-01133-0
nature nanotechnology

Nanostructured block copolymer muscles

Chao Lang[1,2,3], Elisabeth C. Lloyd[2], Kelly E. Matuszewski[2], Yifan Xu[2], Venkat Ganesan[4], Rui Huang[5], Manish Kumar[4,6] and Robert J. Hickey[2,7]✉

High-performance actuating materials are necessary for advances in robotics, prosthetics and smart clothing. Here we report a class of fibre actuators that combine solution-phase block copolymer self-assembly and strain-programmed crystallization. The actuators consist of highly aligned nanoscale structures with alternating crystalline and amorphous domains, resembling the ordered and striated pattern of mammalian skeletal muscle. The reported nanostructured block copolymer muscles excel in several aspects compared with current actuators, including efficiency (75.5%), actuation strain (80%) and mechanical properties (for example, strain-at-break of up to 900% and toughness of up to 121.2 MJ m^{-3}). The fibres exhibit on/off rotary actuation with a peak rotational speed of 450 r.p.m. Furthermore, the reported fibres demonstrate multi-trigger actuation (heat and hydration), offering switchable mechanical properties and various operating modes. The versatility and recyclability of the polymer fibres, combined with the facile fabrication method, opens new avenues for creating multifunctional and recyclable actuators using block copolymers.

Biological tissues are intricately and hierarchically structured for specific functions and provide inspiration for creating novel materials exhibiting remarkable properties[1–4]. For example, natural structural materials such as silk[3], nacre[5], bone and tooth[6] display unique mechanical properties due to their hierarchically ordered hard and soft phases[7]. Beyond static properties, living materials also exhibit energy-efficient and high-precision dynamic responses to the environment[8–10]. A notable example is mammalian skeletal muscles. With the ability to voluntarily generate force or produce movement, skeletal muscles are well-known for their multilevel hierarchical structures, especially the characteristic highly ordered and striated patterns at the single cell (muscle fibre) level[11] (Fig. 1a). Importantly, the actuation performance of muscles is directly related to their structural order, where disorder of the structure leads to drastic failure of function[12].

Inspired by natural muscles, artificial muscles and biomimetic actuators have the potential to revolutionize the fields of robotics[13,14], prosthetic limbs[15] and smart clothing[16–18], leading to their rapid development in recent years[19–22]. While notable progress has been made in terms of replication of the actuating function of muscle fibres[20–24], mimicking the structure–function interplay has been largely ignored. An opportunity in the development of artificial muscles is correlating high-performance actuating materials with structural designs based on natural skeletal muscle fibres. In this respect, nanoscale block copolymer self-assembly is an ideal tool due to its broad structural palette and well-established guiding theories[25,26]. As synthetic strategies and the versatility of chain architectures advance, numerous applications are being developed for bulk and solution-phase nanoscale self-assembled block copolymers[27,28], ranging from daily use in commodities such as adhesives, coatings and packaging[28,29], to highly engineered products such as therapeutic administration[30,31], organic electronics[32,33] and separation membranes[34–36].

Here we report an innovative strategy for developing nanostructured actuating materials that bear surprising resemblance to both the structure and the function of mammalian skeletal muscle fibres. Reversible and recyclable polymer actuators are enabled by the use of nanostructured block copolymers. The combination of solution-phase block copolymer self-assembly and subsequent strain-programmed crystallization (SPC) was used to fabricate a new class of high-performance soft actuator/artificial muscle fibres. The exceptional actuation efficiency, actuation strain and mechanical properties, which have yet to be reported, are attributed to the highly aligned nanometre-scale fibre microstructure, containing alternating crystalline and amorphous domains. Through implantation of both linear and rotational actuation movements with different stimuli-responses, as well as demonstration of continuous and switchable operating modes, we further highlight the versatility and potential of the reported actuating materials.

Fabrication of strained fibres

We adopted a facile two-step fabrication method to create biomimetic actuating fibres. The first step is to prepare uniform hydrogel fibres using the recently described rapid-injection method[37] where a 22 wt% tetrahydrofuran (THF) solution of poly(styrene)-b-poly(ethylene oxide)-b-poly(styrene) (SOS) is injected into a water bath to trigger self-assembly (Fig. 1a,b). The linear ABA-type triblock copolymer SOS was synthesized by sequential living anionic polymerization followed by a coupling step, which afforded polymers with a number-average molecular weight (M_n) of 77 kg mol^{-1}, a poly(ethylene oxide) (PEO) volume fraction of 75% and a low-molecular-weight dispersity ($Đ$) of 1.07 (Supplementary Fig. 1 and Supplementary Table 1). The narrow $Đ$ enables enhanced control over the self-assembly process[38], which is helpful for mimicking the long-range-ordered structure of muscle fibres[39]. Rapid injection is an easy and versatile way for preparing physically crosslinked hydrogels with exceptional mechanical properties and hierarchical structures[37]. The rapid-injection hydrogel fibres are transparent and uniform in diameter (Supplementary Figs. 3 and 5). At the

[1]South China Advanced Institute for Soft Matter Science and Technology, School of Emergent Soft Matter, South China University of Technology, Guangzhou, China. [2]Materials Science and Engineering, The Pennsylvania State University, University Park, PA, USA. [3]Guangdong Provincial Key Laboratory of Functional and Intelligent Hybrid Materials and Devices, South China University of Technology, Guangzhou, China. [4]McKetta Department of Chemical Engineering, The University of Texas at Austin, Austin, TX, USA. [5]Department of Aerospace Engineering and Engineering Mechanics, The University of Texas at Austin, Austin, TX, USA. [6]Department of Civil, Architectural and Environmental Engineering, The University of Texas at Austin, Austin, TX, USA. [7]Materials Research Institute, The Pennsylvania State University, University Park, PA, USA. ✉e-mail: rjh64@psu.edu

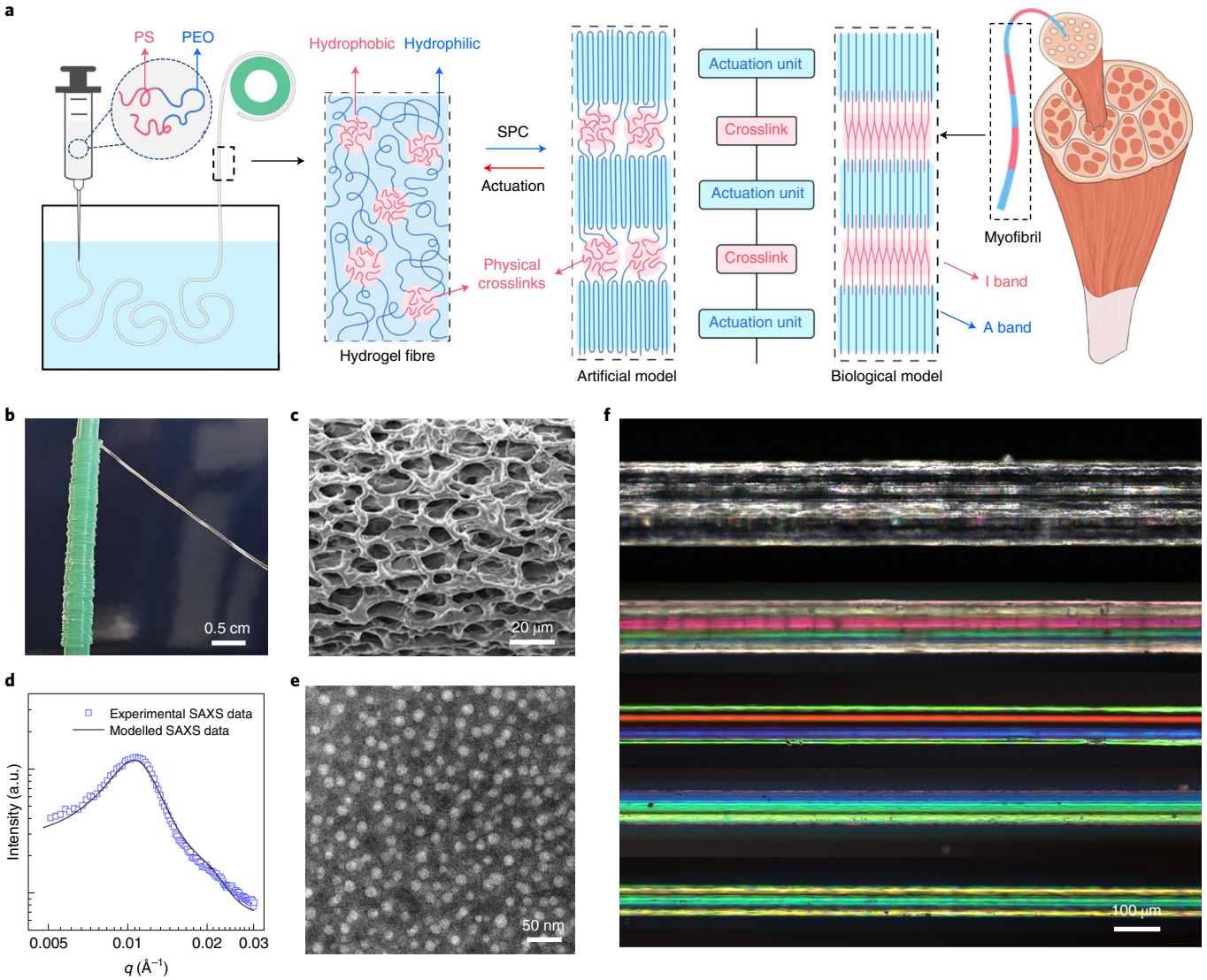

Fig. 1 | Fibre fabrication through SPC of hydrogels created from self-assembled ABA triblock copolymers. a, A scheme depicting the fibre preparation process and structural comparison between an artificial model of SOS fibres and a biological model of muscle myofibrils. **b**, A 1-m-long hydrogel fibre made from rapid-injection processing using an SOS triblock copolymer. The ABA-type polymer chain architecture where the A-end blocks are glassy and the B-midblock is semicrystalline is essential for creating mechanically robust hydrogel fibres[50,51]. **c**, SEM image of a freeze-dried hydrogel fibre, which exhibits interconnected cellular network structures at the micrometre scale. **d**, SAXS data of the hydrogel fibre was modelled using a spherical form factor and a Percus–Yevick structure factor[37], which indicates a structure of a disordered sphere at the nanometre scale. *q*, scattering vector ($Å^{-1}$). **e**, TEM image of the SOS microgel showing disordered spheres resulting from the self-assembly procedure. **f**, DIC images show that the 1×–5× fibres are uniform after crystallization under straining conditions and the alignment of the fibres increases along the fibre axis with increasing elongation ratios.

micrometre scale, scanning electron microscopy (SEM) images of the freeze-dried hydrogel fibres indicate that the polymers form an interconnected cellular network, which forms as a result of the rapid-injection-induced phase separation (Fig. 1c). At the nanometre scale, the as-prepared hydrogels display spherical micelle structures formed by aggregation of the hydrophobic poly(styrene) blocks, which were characterized using small-angle X-ray scattering (SAXS) (Fig. 1d). The scattering pattern was modelled with a spherical form factor and a Percus–Yevick structural factor (Fig. 1d and Supplementary Table 2)[40]. The disordered structures of the crosslinked spherical micelles are also imaged using transmission electron microscopy (TEM) on microgel samples produced from rapid-injection processing (Fig. 1e and Supplementary Fig. 2).

The second step is to strain the elastic hydrogel fibres along the fibre axis at specific extensions and induce O-block crystallization during drying to trap the low-entropy, stretched polymer chain state. The restoring mechanical energy is released when the O-block crystals undergo a melting transition to non-crystalline states on application of specific stimuli. The low O-block melting temperature ($T_m \approx 65\,°C$) and excellent water solubility allow for fabrication of actuating materials with mild stimuli. The exceptional mechanical properties and high elongation-at-break values of the hydrogel fibres provide a wide processing window for controlling the properties of the final products. Here we study fibres with elongation ratios of one (1×) to five (5×) (Fig. 1f and Supplementary Fig. 3). As expected, the diameters of the further processed fibres reduce significantly as the elongation ratio increases. (Fig. 1f and Supplementary Fig. 3). Both SEM and differential interference contrast (DIC) microscopy images indicate that the strained fibres are uniform (Fig. 1f and Supplementary Fig. 3). The two-step

fabrication process to create aligned fibres does not introduce any new chemical crosslinks or additional components into the original ABA triblock copolymer, allowing the self-assembled material to be easily recycled and reused by simply redissolving in a suitable solvent[41]. Additionally, the fabrication process does not require special instruments and is easily scalable using wet-spinning processing, which has been widely applied in industry[42].

We selected SOS as a model block copolymer system to illustrate and exemplify our design principles. Glassy hydrophobic polystyrene (PS) end blocks lead to the formation of nanometre-scale spherical micelles when in water, and serve as strong physical crosslinks. The hydrophilic semicrystalline PEO midblock with a suitable $T_{m,PEO}$ ($T_{m,PEO} < T_{g,PS}$) melts to initiate contractile/rotational actuation, and the amorphous PEO domain will absorb water vapour and lead to expansion. Following the same design principle, we anticipate that there are numerous different polymers that will satisfy these stated requirements, which will further expand the functionality and property range of available soft actuator materials.

Structure characterization of SOS fibres

The crystalline unit cell and lamellar orientation of the strained fibres was established using wide-angle X-ray scattering (WAXS) and SAXS, respectively. The existence of crystalline domains in the fibres was confirmed by differential scanning calorimetry (DSC) (Supplementary Fig. 6). On the first heating ramp, the 1×–5× fibres show similar endothermic peaks around 65 °C, indicating the melting of O-block crystals. The crystallinity of the fibres increases with elongation ratios (Supplementary Fig. 6), which are further confirmed with WAXS (Fig. 2a–g and Supplementary Fig. 7). The O-block crystallinity of the 5× fibre is 77%, which is 12% greater than that of the freeze-dried fibre (Fig. 2g). Two-dimensional (2D) WAXS patterns show no change in the O-block crystal structure throughout different samples (Fig. 2a–d and Supplementary Fig. 7), but demonstrate that the orientation of the crystalline domains increases at the unit cell level with increasing elongation ratios. O-blocks in all the samples crystallized into monoclinic structure with $P2_1/a$ space group (Fig. 2e), which is consistent with previous studies[43,44]. The orientation level of the PEO crystal in the fibres was quantified using Herman's orientation factor, which describes the relationship between the normal direction of a specific plane to a reference direction[45]. Using the fibre axis direction as the reference direction, the Herman's orientation factor of crystal plane (120), $f_{(120)}$, was calculated from the azimuthal intensity plot of the (120) reflection (Fig. 2f). $f_{(120)}$ increased from 0 for the freeze-dried fibre to −0.46 for the 5× fibre, indicating that the polymer chain alignment in the crystal structure increases with increasing elongation along the fibre axis (Supplementary Table 3).

SAXS measurements were also performed on the fibres to study O-crystals at the lamellar level (Fig. 2i,j and Supplementary Fig. 8). Variable-temperature experiments indicate that the crystals melt between 60 and 70 °C (Supplementary Figs. 9 and 10), which is consistent with the DSC measurements. The lamellar orientation of the fibres exhibits the same trend as the orientation of the crystal unit cell, which increases with increasing elongation ratios (Fig. 2i,j and Supplementary Fig. 8). By calculating the Herman's orientation factor of the lamellae, f_{lam}, we found the lamellar orientation changed from isotropic for freeze-dried fibre to perpendicular to the fibre axis for 5× fibre (Fig. 2k), which is consistent with the evolving trend of $f_{(120)}$ from WAXS results. The 1D SAXS scattering data also indicate that the lamellar domain spacing increased significantly from 25.1 nm for freeze-dried to 39.6 nm for 5× fibre (Fig. 2k). Combined with the O-block volume fraction in the SOS polymer and O-block crystallinity values, the thickness of the amorphous region of 1×–5× fibre was calculated to vary between 15.6 and 17.8 nm. The domain size of the amorphous region corresponds well with the S-micelle core size of 16.1 nm observed by TEM (Fig. 1e). Figure 2h depicts the proposed structural arrangement of glassy PS cores in the fibre, where the alternating O-crystalline domains and glassy S cores are orientated along the fibre axis. The existence of the PS spheres was first demonstrated through SAXS characterization of the fibres after melting the O-crystalline domains (Supplementary Fig. 11). The fibre structure is further supported by SEM images of the post-stretched fibres, where different layers of S spheres were distinguishable in the fibre (Supplementary Fig. 4). The fascinating structural arrangement of S spheres with O-crystals is not only reminiscent of composite materials in which nanoparticles are embedded in a semicrystalline polymer matrix[46], but also simulates the striated appearance of skeletal muscle fibres. The striated pattern of muscle fibre is a result of lateral alignment of myofibrils, where highly ordered alternating dark (anisotropic, A) and light (isotropic, I) bands can be observed. The repeating unit between neighbouring centres of I bands (Z disks) is defined as the sarcomere, the length of which will change accordingly when the muscle fibres contract or are stretched[47,48]. Similarly, in the strained SOS fibres, the crystalline domains melt under mild heating conditions, which will lead to the neighbouring amorphous domains approaching each other and generating contraction forces (Fig. 1a).

Mechanical and actuation properties of SOS fibres

Uniaxial tensile measurements were conducted to establish the mechanical properties of the 1×–5× fibres (Fig. 3a and Supplementary Fig. 13). The Young's modulus of the fibres increased significantly after the SPC procedure, ranging from 353 to 608.2 MPa, which is over four orders of magnitude greater than that of the precursor hydrogel fibre (0.014 MPa) (Supplementary Table 4). The elongation strains at break and the strengths of the fibres were found to vary with the strain programming elongation ratios. From 1× to 5× fibre, the elongation strain at break decreased from 900% to 170%, where the tensile strength increased from 15.5 to 146.2 MPa (Supplementary Table 4). As a result, the 1×–5× fibres have similar toughness in the range from 103.2 to 121.2 MJ m^{-3}. These values are comparable to that of spider silk (70–160 MJ m^{-3}), which is characterized by extraordinary toughness and biodegradability[3].

The mechanical properties of 1×–5× fibres were modelled using a composite microstructure consisting of three phases (for example, crystalline PEO, amorphous PEO and glassy PS (Supplementary Fig. 15a)) and compared with experimental data (Fig. 3b and Supplementary Figs. 15 and 16). From 1× to 5×, the increase in crystallinity combined with the decrease in porosity (Supplementary Fig. 14) led to a decrease in fibre volume. Through the composite model, the Young's modulus values of the fibres are calculated considering the effects of crystallinity (Supplementary Fig. 15b) and crystal orientation (Supplementary Fig. 16b). The elongation at break and strength values were calculated based on the assumption that the true stress and total strain required to break the fibres are constants. The modelled data agreed well with the experimental data (Fig. 3b and Supplementary Fig. 16b).

We then evaluated the actuation properties of 1×–5× fibres by first investigating the length change during contraction (without loading or attachment). We found that when heating is applied, the strained fibres contract to the expected theoretical value with actuation strains ranging from 0% to ~80% (Fig. 3c and Supplementary Fig. 20a). In comparison, when hydration was used as a stimulus, the strained fibres can display either expansion or contraction strain within the range from about −30% to 70% (Fig. 3c). This wide and tunable actuation range offers opportunities for various engineering applications, including the synthetic mimicry of natural muscle fibres, which contract 40% when isolated and 20% when attached (Supplementary Table 5)[49]. Another noticeable feature is that the fibres display very different mechanical properties (Supplementary Table 4) after actuation, which provides another dimension for

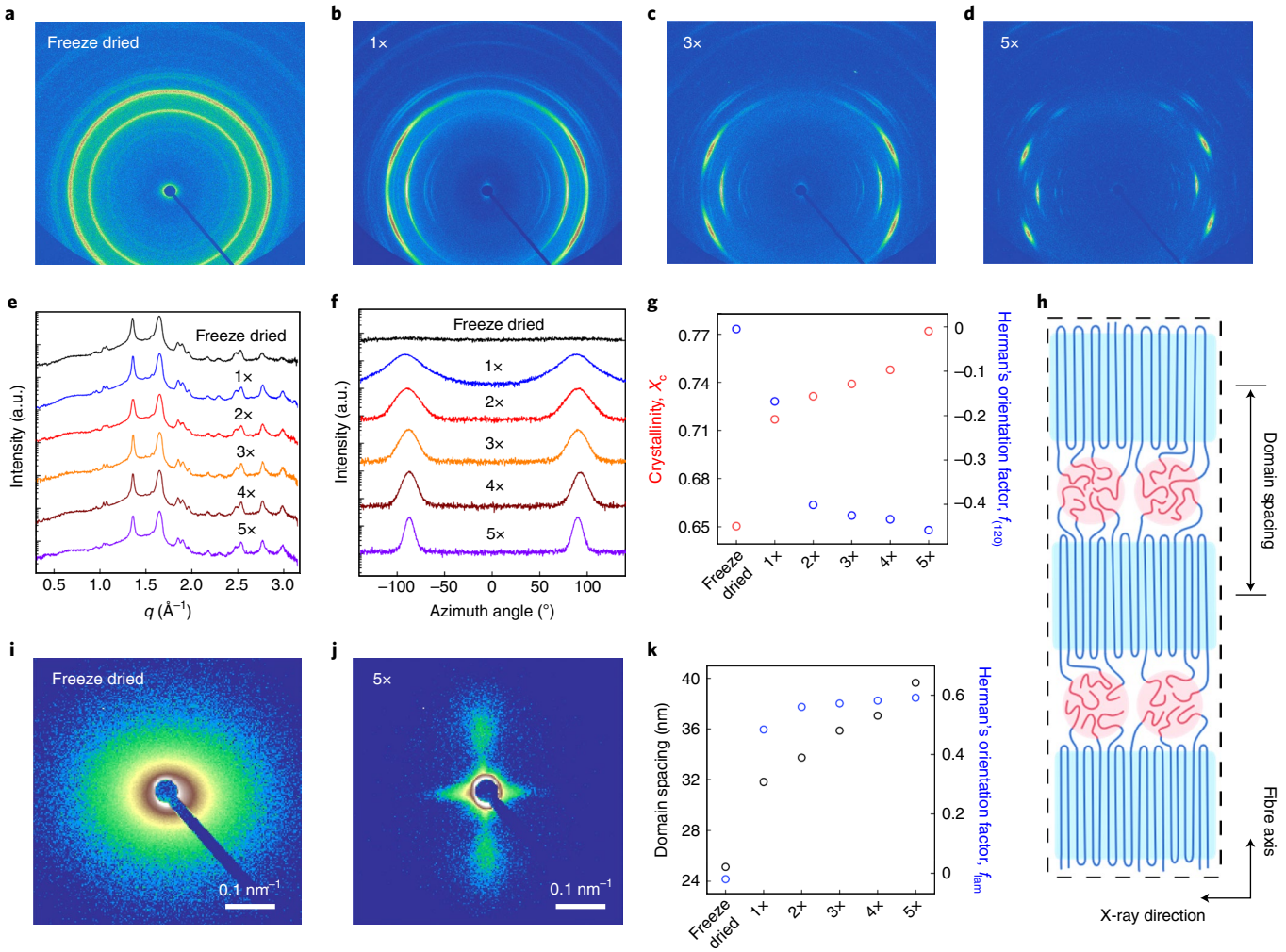

Fig. 2 | SAXS and WAXS characterizations of strain-processed fibres indicate that the structure is highly aligned and consists of alternating crystalline and amorphous domains. a–d, Two-dimensional WAXS scattering results show that freeze-dried (**a**), 1× (**b**), 3× (**c**) and 5× (**d**) fibres exhibit diffraction patterns characteristic of O-block crystals. The crystal orientation in the fibre increases with increasing elongation ratio. **e**, One-dimensional WAXS scattering of fibres at different strains plotted together show the same crystal unit structure of O. **f**, One-dimensional scattering profiles from azimuthal angle integration of the 2D WAXS data indicate that the crystal orientation at unit-cell level in the fibres increases with increasing elongation ratio. **g**, From freeze-dried to 5× fibre, the crystallinity, X_c, increases and the Herman's orientation factor of the crystal plane (120), $f_{(120)}$, decreases from 0 to −0.46, suggesting that the (120) plane becomes increasingly parallel to the fibre direction. **h**, A scheme showing the suggested fibre structure with alternating crystalline and amorphous domains. **i**,**j**, Two-dimensional SAXS patterns of freeze-dried and 5× fibres indicate that the crystal orientation at the lamellar level increases with increasing elongation ratio. **k**, Changes in domain spacing and the Herman's orientation factor of the lamellae, f_{lam}, of fibres with increasing extension ratio, indicating that the orientation of the crystal lamellae become increasingly perpendicular to the fibre axis from freeze-dried to 5× fibres.

engineering design. For example, contracted fibres are either solid and rigid after heating-triggered actuation due to the recrystallization of the O-domains when cooled back to room temperature, or soft and elastic, similar to the starting hydrogel fibre, after hydration (Fig. 3g). The actuation stress generated by the fibres was then quantified using a load frame, which also shows an increasing trend from 1× to 5× (Fig. 3d). The 5× fibres can deliver an actuation stress of 5.5 MPa, which is 15 times greater than that delivered by natural muscle fibres (Supplementary Table 5)[49].

To quantify the work capacity of the strained fibres, weight-lifting tests were performed (Fig. 3e,f and Supplementary Fig. 18). The actuation movement was quantified in detail through video analysis (Fig. 3e, Supplementary Fig. 18 and Supplementary Videos 1 and 2). As expected, both the actuation strain and peak actuation speed of the fibres increase with increased elongation ratios (Fig. 3e and Supplementary Fig. 18). Furthermore, the acceleration time was short, indicating that stored energy is rapidly released during actuation. Notably, the 5× fibres exhibit an actuation strain of 70% even when lifting an object greater than 700 times the fibre weight. Based on the same composite microstructure model for mechanical properties, the theoretical value of actuation strain triggered by heating was also calculated and exhibited the same trend as the experimental values (Supplementary Fig. 20). The energy density was then evaluated using the work done by the fibres and the fibre weight (Fig. 3f). All fibres exhibit high energy density, but the 5× fibre reaches a maximum of 506 J kg^{-1} in the series, which is more than ten times greater than that of mammalian skeletal muscle (39 J kg^{-1}) (Supplementary Table 5). Notably, these fibres exhibit actuation behaviours with high energy efficiency ranging from 40.5% to 75.5% with hydration as a stimulus (Supplementary Fig. 19), which is one of the highest among reported soft actuator/artificial muscle materials (Supplementary Table 5). The radar

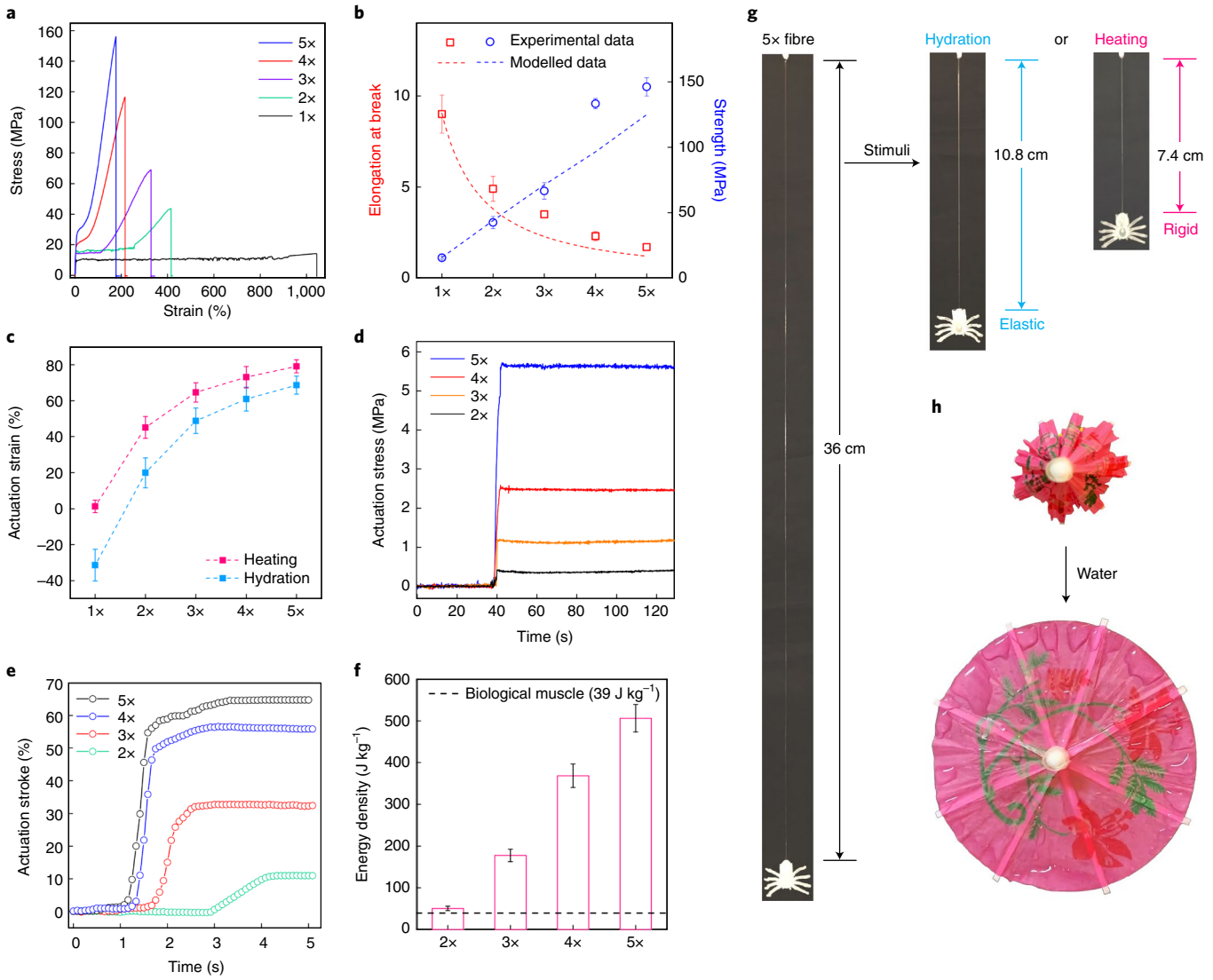

Fig. 3 | Strained fibres exhibit exceptional mechanical and actuation properties. a, Stress versus strain (%) results of the fibres show decreased elongation at break values and increased tensile strength from 1× to 5×. Strain rate, 3 min^{-1}. **b**, Comparison of experimental and modelled mechanical properties of 1×–5× fibres. **c**, Length change of the fibres with different stimuli, where heating leads to contraction strains ranging from 0% to ~80%, and hydration leads to either expansion or contraction strains from about −30% to 70%. **d**, The contractile actuation stress generated by 2×–5× fibres with hydration as the stimuli. **e**, Actuation strain of the fibre with hydration as the stimulus while lifting a weight (0.31 g) that is more than 700 times the 5× fibre's own weight. **f**, Energy density of 2×–5× fibres compared with mammalian skeletal muscle (39 J kg^{-1}). These values were calculated from fibres lifting a weight of 0.31 g. **g**, Photographs of 5× fibres before and after actuation. A small weight on the bottom of the fibre is used as a visual aid to help assess the fibre contraction. The 5× fibres generate large actuation strains with both hydration and heating as stimuli, but display different mechanical properties after actuation. **h**, An umbrella that autonomously opens when water is applied. 5× fibres were attached to the umbrella ribs for actuation.

figure in Supplementary Fig. 22 demonstrates a multidimensional comparison of material performance metrics for the reported fibres and previously published works on actuating artificial muscles. The reported nanostructured fibres outperform current actuating fibres in many respects, including tensile strain, toughness, actuation strain and efficiency. To further demonstrate the versatility of the fibres, an umbrella that automatically opens when applying water was developed by simply attaching 5× fibres to the umbrella ribs (Fig. 3h and Supplementary Video 3).

Reversible and rotational actuation behaviours of SOS fibres

The reversible actuation behaviours of the fibres were then characterized by partially melting the crystalline domains via heating at fixed fibre length (that is, constant strain). By controlling the heating temperature and time, 5× fibres were shown to generate a reversible contractile stress, where more than 100 actuation cycles were demonstrated without any loss of performance (Fig. 4a). The results indicate the potential of further applying these block copolymer fibres in real-world applications. Beyond contraction, we also found that the strained fibres can perform expansional actuation in a cyclic manner. When the relative humidity in the environment was varied (Supplementary Fig. 21), the amorphous regions of the fibres can reversibly absorb and deabsorb water vapour, causing the fibre to generate reversible expansion stress (Fig. 4b). Here, water vapour is treated as a different stimulus to hydration due to the opposite actuation responses of the SOS fibres and mechanisms. Specifically, strained fibres exposed to water vapour for short periods (for example, several seconds for our actuation experiment) expanded due to the water molecules swelling the amorphous PEO

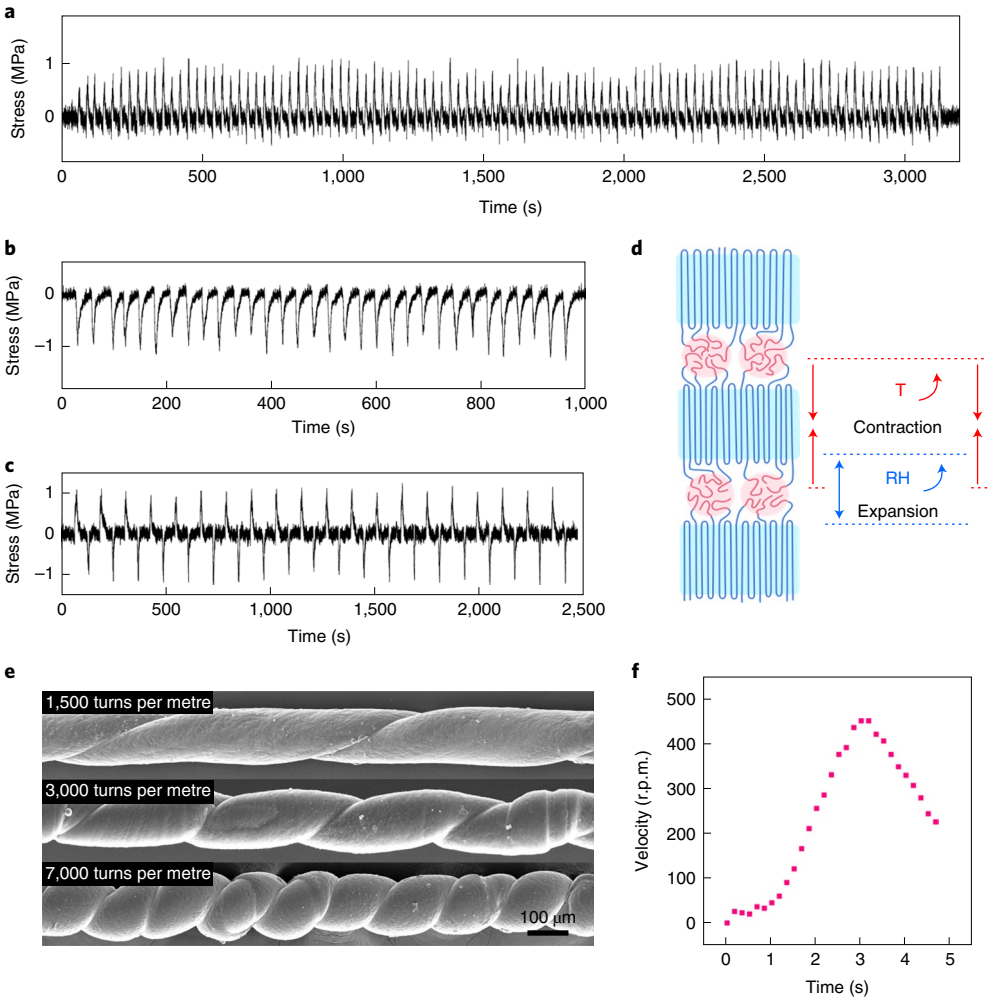

Fig. 4 | Reversible and rotational actuation properties of strained fibres. a, Reversible contractile actuation stress generation from 5× fibre at fixed length with heating as the stimulus. **b**, Reversible expansional actuation stress generation from 5× fibre at fixed length by swelling and deswelling of the amorphous domains with water vapour. **c**, Alternating contractile and expansional actuation stress generation from 5× fibre at fixed length controlled by heating and water vapour. **d**, A scheme displaying the mechanism of reversible actuation behaviours of the fibres triggered by heating (T) and water vapour (RH). **e**, SEM of fibres with different twist degrees per length. **f**, Rotational velocity from SOS fibre with a twist degree of 7,000 turns per metre where heating was used as a stimulus.

regions but not melting the crystals. However, when the fibre sample is fully immersed in water (hydration), the PEO crystals melt, and the polymer fibres (2×–5×) contract due to the highly anisotropic nature of the structures. When both stimuli were used together, the fibres can generate either contraction or expansion stress as desired (Fig. 4c), making them more versatile actuators than natural muscle fibres (Fig. 4d). This dual-action feature is particularly appealing for building multimodal locomotive robots for completing tasks in complicated environments[14].

In addition to linear actuators made through straining, we also prepared rotational actuators by twisting the hydrogel fibres before crystallization. SEM images show that the rotational angles of the helical fibres can be tuned by controlling the twist degree (Fig. 4e). Similar to the linear actuators, rotational actuation is triggered via either hydration or heating (Fig. 4f), which was found to operate in continuous and switchable modes, respectively. Under hydration, the actuator works in a continuous fashion where constant rotational actuation will sustain until full energy release (Supplementary Video 4). A peak rotational speed of 450 r.p.m. was observed. Alternatively, heating offers better control: actuation can be easily switched between on and off by applying or removing heating (Supplementary Video 5). The rotational actuator is a demonstration of the versatility of this new type of actuating material. In our previous study[37], we showed that rapid injection can be used for preparing hydrogels in different configurations such as coatings, printings, composites and complex objects. We thus envision that the two-step fabrication process is easily translated to many application scenarios where tough, high-performance, light-weight and recyclable actuating materials are required.

Conclusions

Inspired by the structure and the function of muscle fibres, fibre actuators with highly aligned alternating amorphous and crystalline domains were prepared from ABA triblock copolymers. The glassy and semicrystalline properties of the A and B blocks, respectively, which are necessary to mimic the structure and function of skeletal muscles, are easily translatable to different polymer compositions to satisfy materials requirements for specific applications. The fibres were fabricated using a two-step method, where hydrogel fibres made from rapid-injection processing were crystalized under strain to trap a low-entropy state. The fibres are recyclable due to a lack of chemical crosslinks, and yet display excellent mechanical

properties, with toughness rivalling that of spider silk. The fibres also exhibit exceptional actuation behaviours, where the actuation strain, stress, energy density and energy efficiency not only exceed the natural muscle fibres, but are also easily tuned. The reported nanostructured block copolymer fibres demonstrate both linear and rotational actuation movements that are triggered from three different stimuli (for example, expansion in water vapour, and contraction/rotation in heating or hydration). Potential applications of such fibres include surgical robots, smart clothes, haptic and tactile interfaces, and prostheses.

Online content

Any methods, additional references, Nature Research reporting summaries, source data, extended data, supplementary information, acknowledgements, peer review information; details of author contributions and competing interests; and statements of data and code availability are available at https://doi.org/10.1038/s41565-022-01133-0.

Received: 6 October 2021; Accepted: 2 April 2022;
Published online: 2 June 2022

References

1. Vukusic, P. & Sambles, J. R. Photonic structures in biology. *Nature* **424**, 852–855 (2003).
2. Hamm, C. E. et al. Architecture and material properties of diatom shells provide effective mechanical protection. *Nature* **421**, 841–843 (2003).
3. Omenetto, F. G. & Kaplan, D. L. New opportunities for an ancient material. *Science* **329**, 528–531 (2010).
4. Wong, T.-S. et al. Bioinspired self-repairing slippery surfaces with pressure-stable omniphobicity. *Nature* **477**, 443–447 (2011).
5. Tang, Z., Kotov, N. A., Magonov, S. & Ozturk, B. Nanostructured artificial nacre. *Nat. Mater.* **2**, 413–418 (2003).
6. Hannig, M. & Hannig, C. Nanomaterials in preventive dentistry. *Nat. Nanotechnol.* **5**, 565–569 (2010).
7. Wegst, U. G. K., Bai, H., Saiz, E., Tomsia, A. P. & Ritchie, R. O. Bioinspired structural materials. *Nat. Mater.* **14**, 23–36 (2015).
8. Bell, F. I., McEwen, I. J. & Viney, C. Supercontraction stress in wet spider dragline. *Nature* **416**, 37–37 (2002).
9. Capadona, J. R., Shanmuganathan, K., Tyler, D. J., Rowan, S. J. & Weder, C. Stimuli-responsive polymer nanocomposites inspired by the sea cucumber dermis. *Science* **319**, 1370–1374 (2008).
10. He, X. et al. Synthetic homeostatic materials with chemo-mechano-chemical self-regulation. *Nature* **487**, 214–218 (2012).
11. Lieber R. L. *Skeletal Muscle Structure, Function, and Plasticity* 2nd edn (Lippincott Williams & Wilkins, 2002).
12. Puthucheary, Z., Montgomery, H., Moxham, J., Harridge, S. & Hart, N. Structure to function: muscle failure in critically ill patients. *J. Physiol.* **588**, 4641–4648 (2010).
13. Li, C. et al. Fast and programmable locomotion of hydrogel–metal hybrids under light and magnetic fields. *Sci. Robot.* **5**, eabb9822 (2020).
14. Hu, W., Lum, G. Z., Mastrangeli, M. & Sitti, M. Small-scale soft-bodied robot with multimodal locomotion. *Nature* **554**, 81–85 (2018).
15. Biddiss, E. & Chau, T. Dielectric elastomers as actuators for upper limb prosthetics: challenges and opportunities. *Med. Eng. Phys.* **30**, 403–418 (2008).
16. Wang, W. et al. Harnessing the hygroscopic and biofluorescent behaviors of genetically tractable microbial cells to design biohybrid wearables. *Sci. Adv.* **3**, e1601984 (2017).
17. Eschen, K., Granberry, R. & Abel, J. Guidelines on the design, characterization, and operation of shape memory alloy knitted actuators. *Smart Mater. Struct.* **29**, 035036 (2020).
18. Zhao, H. et al. Wearable sunlight-triggered bimorph textile actuators. *Nano Lett.* **21**, 8126–8134 (2021).
19. Mirvakili, S. M. & Hunter, I. W. Artificial muscles: mechanisms, applications, and challenges. *Adv. Mater.* **30**, 1704407 (2018).
20. Kanik, M. et al. Strain-programmable fiber-based artificial muscle. *Science* **365**, 145–150 (2019).
21. Mu, J. et al. Sheath-run artificial muscles. *Science* **365**, 150–155 (2019).
22. Yuan, J. et al. Shape memory nanocomposite fibers for untethered high-energy microengines. *Science* **365**, 155–158 (2019).
23. Chen, P. et al. Hierarchically arranged helical fibre actuators driven by solvents and vapours. *Nat. Nanotechnol.* **10**, 1077–1083 (2015).
24. Liu, D. et al. Spider dragline silk as torsional actuator driven by humidity. *Sci. Adv.* **5**, eaau9183 (2019).
25. Bates, F. S. & Fredrickson, G. Block copolymers—designer soft materials. *Phys. Today* **52**, 32–38 (1999).
26. Bates, F. S. et al. Multiblock polymers: panacea or Pandora's box? *Science* **336**, 434–440 (2012).
27. Mai, Y. & Eisenberg, A. Self-assembly of block copolymers. *Chem. Soc. Rev.* **41**, 5969–5985 (2012).
28. Bates, C. M. & Bates, F. S. 50th anniversary perspective: block polymers—pure potential. *Macromolecules* **50**, 3–22 (2017).
29. Shin, J. et al. Pressure-sensitive adhesives from renewable triblock copolymers. *Macromolecules* **44**, 87–94 (2011).
30. Jeong, B., Bae, Y. H., Lee, D. S. & Kim, S. W. Biodegradable block copolymers as injectable drug-delivery systems. *Nature* **388**, 860–862 (1997).
31. Geng, Y. et al. Shape effects of filaments versus spherical particles in flow and drug delivery. *Nat. Nanotechnol.* **2**, 249–255 (2007).
32. Bouchet, R. et al. Single-ion BAB triblock copolymers as highly efficient electrolytes for lithium–metal batteries. *Nat. Mater.* **12**, 452–457 (2013).
33. Cho, J. H. et al. Printable ion-gel gate dielectrics for low-voltage polymer thin-film transistors on plastic. *Nat. Mater.* **7**, 900–906 (2008).
34. Tu, Y.-M. et al. Rapid fabrication of precise high-throughput filters from membrane protein nanosheets. *Nat. Mater.* **19**, 347–354 (2020).
35. Phillip, W. A. et al. Tuning structure and properties of graded triblock terpolymer-based mesoporous and hybrid films. *Nano Lett.* **11**, 2892–2900 (2011).
36. Peinemann, K.-V., Abetz, V. & Simon, P. F. W. Asymmetric superstructure formed in a block copolymer via phase separation. *Nat. Mater.* **6**, 992–996 (2007).
37. Lang, C. et al. Solvent-non-solvent rapid-injection for preparing nanostructured materials from micelles to hydrogels. *Nat. Commun.* **10**, 3855 (2019).
38. Lynd, N. A., Meuler, A. J. & Hillmyer, M. A. Polydispersity and block copolymer self-assembly. *Prog. Polym. Sci.* **33**, 875–893 (2008).
39. Li, M.-H., Keller, P., Yang, J. & Albouy, P.-A. An artificial muscle with lamellar structure based on a nematic triblock copolymer. *Adv. Mater.* **16**, 1922–1925 (2004).
40. Taribagil, R. R., Hillmyer, M. A. & Lodge, T. P. Hydrogels from ABA and ABC triblock polymers. *Macromolecules* **43**, 5396–5404 (2010).
41. Garcia, J. M. & Robertson, M. L. The future of plastics recycling. *Science* **358**, 870–872 (2017).
42. Kou, L. et al. Coaxial wet-spun yarn supercapacitors for high-energy density and safe wearable electronics. *Nat. Commun.* **5**, 3754 (2014).
43. Zhu, L. et al. Crystallization temperature-dependent crystal orientations within nanoscale confined lamellae of a self-assembled crystalline–amorphous diblock copolymer. *J. Am. Chem. Soc.* **122**, 5957–5967 (2000).
44. Takahashi, Y. & Tadokoro, H. Structural studies of polyethers, $(-(CH_2)_m-O-)_n$. X. Crystal structure of poly(ethylene oxide). *Macromolecules* **6**, 672–675 (1973).
45. Ponçot, M. et al. Complementarities of high energy WAXS and Raman spectroscopy measurements to study the crystalline phase orientation in polypropylene blends during tensile test. *Polymer* **80**, 27–37 (2015).
46. Zhao, D. et al. Tunable multiscale nanoparticle ordering by polymer crystallization. *ACS Cent. Sci.* **3**, 751–758 (2017).
47. Rall, J. A. What makes skeletal muscle striated? Discoveries in the endosarcomeric and exosarcomeric cytoskeleton. *Adv. Physiol. Educ.* **42**, 672–684 (2018).
48. Schneidereit, D. et al. Optical prediction of single muscle fiber force production using a combined biomechatronics and second harmonic generation imaging approach. *Light Sci. Appl.* **7**, 79 (2018).
49. Madden, J. D. W. et al. Artificial muscle technology: physical principles and naval prospects. *IEEE J. Ocean. Eng.* **29**, 706–728 (2004).
50. Lang, C. et al. Biomimetic separation of transport and matrix functions in lamellar block copolymer channel-based membranes. *ACS Nano* **13**, 8292–8302 (2019).
51. Lang, C., Kumar, M. & Hickey, R. J. Influence of block sequence on the colloidal self-assembly of poly(norbornene)–block–poly(ethylene oxide) amphiphilic block polymers using rapid injection processing. *Polym. Chem.* **11**, 375–384 (2020).

Methods

Synthesis and characterization of SOS. The triblock SOS copolymers used in this study were synthesized by sequential living anionic polymerization followed by coupling the hydroxyl groups at the PEO end with α,α′-dibromo-*p*-xylene[37]. The synthesized polymers were characterized by NMR (Avance AV3HD 500 NMR spectrometer, Bruker) and size-exclusion chromatography (EcoSEC HLC-8320GPC, Tosoh Bioscience) with THF as the mobile phase. The size-exclusion chromatograph was equipped with a Wyatt DAWN Heleos-II eight-angle static light scattering detector (Wyatt Technology).

Procedure for fibre preparation. The fibres were prepared by a two-step fabrication process. The first step is to make hydrogel fibres using rapid-injection processing[37], which is a solution-phase self-assembly method for amphiphilic block polymers. The second step is a subsequent strain-programmed crystallization of the hydrogel fibres. The details of a typical fibre fabrication procedure are as follows. A 22 wt% THF solution of SOS was first injected into an excess amount of water through a nozzle with an inner diameter of 0.51 mm at an injection rate of 5 ml min^{-1}, leading to the formation of hydrogel fibres. The hydrogel fibres were then strained at different elongation ratios, λ, ranging from 1 to 5 ($\lambda = L_S/L_0$, where L_0 and L_S are the initial and final length of the hydrogel fibres, respectively; the strain rate was 3 min^{-1}). The fibres were then allowed to dehydrate and crystallize at ambient conditions under constant strain with both ends marked and fixed, leading to 1×–5× samples with different degrees of strain programmed into the fibre. The freeze-dried fibres were prepared by quenching the hydrated hydrogel fibres into liquid nitrogen and freeze dried under high vacuum to preserve the hydrogel network backbone structure. The helical fibres were fabricated by fixing one end of the fibre and rotating the other end until the desired twist degree was reached. Both ends of the fibre were then fixed and the fibre was allowed to dehydrate and crystallize at ambient conditions.

DSC. The thermal properties of the fibres were characterized by DSC using a Thermal Analysis Q2000. To prepare the samples, approximately 5 mg of fibres was loaded into hermetic aluminium pans. Data from the first heating ramp under nitrogen atmosphere were collected. The samples were first equilibrated at 25 °C and then heated to 100 °C at a heating rate of 10 °C min^{-1}. The crystallinity of the sample was calculated using the following equation:

$$X_{c,SOS} = \frac{H_m}{H_m^{\infty}} \tag{1}$$

where H_m is measured heat of fusion and H_m^{∞} is the heat of fusion for an infinite PEO crystal (203 J g^{-1}). The crystallinity of the PEO can be further calculated using the following equation:

$$X_{c,PEO} = \frac{H_m}{H_m^{\infty}} \times \frac{1}{w_{PEO}} \tag{2}$$

where w_{PEO} is the weight fraction of PEO in block copolymer SOS.

X-ray scattering. Transmission SAXS and WAXS measurements of the freeze-dried and 1×–5× fibre samples were performed using a Cu Kα source (1.54 Å and 8.04 keV) Xeuss 2.0 (XENOCS) instrument fitted with collimation optics and a 2D X-ray detector (Pilatus3R 200K-A, Dectris). The scattering wavevector, q, was calibrated by using a standard sample of powder silver behenate. The fibres were placed vertically and measured under vacuum.

Synchrotron measurements were conducted at National Synchrotron Light Source II (NSLS-II) at Brookhaven National Laboratory on the Complex Materials Scattering (CMS/11-BM) beamline. Using a 13.50 keV beam (where the wavelength was 0.9184 Å), the hydrogel samples were exposed for 10 s at ambient conditions and artificial muscle fibres were exposed for 3 s under vacuum. The scattering images were captured with a Dectris Pilatus 2M detector; the sample-to-detector distance was 5 m.

Crystal orientation. The orientation levels of the PEO crystal in different fibre samples were quantified by the orientation factor $\langle\cos^2\varphi\rangle$ and Herman's orientation factor f using the following equations:

$$\left\langle \cos^2\varphi \right\rangle = \frac{\int_0^{\frac{\pi}{2}} I(\varphi)\cos^2\varphi\sin\varphi \mathrm{d}\varphi}{\int_0^{\frac{\pi}{2}} I(\varphi)\sin\varphi \mathrm{d}\varphi} \tag{3}$$

$$f = \frac{3\left(cos^2\varphi\right) - 1}{2} \tag{4}$$

where $I(\varphi)$ is the scattering intensity by the (hkl) plane as a function of the azimuthal angle φ (relative to the reference direction). Significant values of $\langle\cos^2\varphi\rangle$ and f are included in Supplementary Table 3.

Modelling of the SAXS data. The SAXS data of hydrogel fibres and artificial muscle fibres were modelled using previously reported methods[37,40,52]. For 1× and 2×, the samples were heated above the melting temperature of PEO with both ends of the fibres fixed to only characterize the structure of the PS spheres. For the hydrogel samples, due to the low scattering length density difference between polystyrene (ρ_{PS}, 9.516 × 10^{10} cm^{-2}) and water (ρ_{water}, 9.441 × 10^{10} cm^{-2}), the scattering pattern of the hydrogel fibre was mainly attributed to the difference between the high PEO concentration in the micelle corona and the low PEO concentration in the hydrogel matrix. Similar to previous work[37,40,52], the scattering intensity profile can be simulated as the product of the hard sphere form $P(q)$ and the disordered spherical structure factor, $S(q)$. The fitting parameters used in the model are listed in Supplementary Table 2.

Tensile test. Uniaxial tensile stress–strain tests were performed on an Instron 5866 load frame with a 10 N load cell. The samples were stretched at a constant strain rate of 3 min^{-1} until fracture, and measurements were conducted in triplicate for each sample. The mechanical properties of the fibres are summarized in Supplementary Table 4. The data obtained from the instrument were background-subtracted. The Young's modulus of the 1×–5× samples can be evaluated by fitting the initial part of the stress–strain curves using the following equation:

$$\sigma_{eng} = E\varepsilon_{eng} \tag{5}$$

where σ_{eng} is the engineering stress, ε_{eng} is the engineering strain and E is Young's modulus. The Young's modulus of the hydrogel sample can be evaluated by fitting the initial part of the stress–strain curves using the following equation:

$$\sigma_{eng} = \frac{E}{3}\left(\lambda - \frac{1}{\lambda^2}\right) \tag{6}$$

where $\lambda = 1 + \varepsilon_{eng}$ is the elongation ratio. In addition, the maximum engineering stress was taken as the strength, and the toughness was calculated by integrating the stress–strain curves.

Measurement of fibre actuation stress. To measure the stress generated by the fibres during actuation, both ends of a 2-cm-long fibre were fixed to sample holders of the load frame, where one of the holders was attached to a fixed surface and the other one attached to the force transducer. While maintaining the distance between the two holders constant, water was applied to the fibre through spraying. The force reading from the transducer was then reordered, which can be further converted to stress using the initial cross-section area of the fibres. Measurements were conducted in triplicate for each sample (Supplementary Fig. 17).

Fibre actuation movement quantification. The linear actuation movements of the fibres were quantified using the video analysis and modelling tool, Tracker 5.1.x (The Open Source Physics Project). The hanging weight was marked for movement tracking. The length scale of the video footage was first calibrated, and the marker position was set as the coordinate origin before the video was analysed frame by frame. The rotational movement was quantified by analysing the video with MATLAB code provided by MathWorks with minor modification. The rotational velocity was obtained by tracking the HSV colour value changing times per frame, which can be then converted to rotations per minute using the frame rate of the video. The energy density was then calculated by using the work done by the fibre divided by the fibre mass. The energy efficiency of the fibres was estimated using the work performed by the fibre divided by the mechanical energy input during fibre straining, which can be characterized by tensile testing (Supplementary Fig. 13). Heating was applied using ceramic ionic flat irons (HSI Professional Glider), while water vapour was applied through polyurethane sponge strips. Hydration was applied by either submerging the sample into water with a glass cylinder (for contraction) or adding water to the sample with a syringe (for rotation).

Data availability

The datasets that support the finding of this study are available in ScholarSphere repository with the identifier(s) https://doi.org/10.26207/tvbb-rf14. Source data are provided with this paper.

References

52. Guo, C. & Bailey, T. S. Highly distensible nanostructured elastic hydrogels from AB diblock and ABA triblock copolymer melt blends. *Soft Matter* **6**, 4807–4818 (2010).

Acknowledgements

This work was supported by the Air Force Office of Scientific Research under the Young Investigator Prize (award 18RT0680, R.J.H.), the National Science Foundation through the DMREF programme (CMMI 2119717, R.J.H.) and the Materials Research Institute seed grant from The Pennsylvania State University (R.J.H.). M.K. was supported by National Science Foundation grant CBET 1946392 and DMREF programme CMMI 1627197. V.G. was supported in part by the Welch Foundation (grant F-1599). This research used the Complex Materials Scattering beamline of the National Synchrotron Light Source II, a US Department of Energy (DOE) Office of Science User Facility

operated for the DOE Office of Science by Brookhaven National Laboratory under contract number DE-SC0012704. TEM, SEM, SAXS and WAXS measurements were taken at the Materials Characterization Lab (MCL) in the Materials Research Institute (MRI) at The Pennsylvania State University.

Author contributions

C.L., M.K. and R.J.H. conceived the research. C.L. developed, prepared and characterized materials. C.L. measured mechanical and actuation properties. E.C.L. and Y.X. conducted X-ray measurements. C.L. and K.E.M. analysed actuation properties using video analysis. V.G. and R.H. developed the mechanical property model. C.L., M.K. and R.J.H. wrote the manuscript. R.J.H. supervised the research. All authors read and commented on the manuscript.

Competing interests

The authors declare no competing interests.

Additional information

Supplementary information The online version contains supplementary material available at https://doi.org/10.1038/s41565-022-01133-0.

Correspondence and requests for materials should be addressed to Robert J. Hickey.

Peer review information *Nature Nanotechnology* thanks Xuanhe Zhao and the other, anonymous, reviewer(s) for their contribution to the peer review of this work.